magnetochemistry

MDPI

Article

Theoretical Study of Pentacoordinated Lanthanide Single-Ion Magnets via Ab Initio Electronic Structure Calculation

Yu-Xi Wang, Yu-Fei Wang and Bing Yin *

Key Laboratory of Synthetic and Natural Functional Molecule of the Ministry of Education, Lab of Theoretical Molecular Magnetism, College of Chemistry and Materials Science, Northwest University, Xi'an 710127, China
* Correspondence: rayinyin@nwu.edu.cn

Abstract: A theoretical study, based on ab initio electronic structure calculation, is performed in a group of 16 pentacoordinate Dy-SIMs. Theoretical results provide a reasonable explanation of the observed SMM performance based on a concise criterion, i.e., the coexistence of long τ_{QTM} and high U_{eff}. To have the desired electronic structure favoring good SMM performance, the contribution from the equatorial coordinating atoms might be even more important than that from the axial coordinating atoms. Widening the axial ∠O–Dy–O might be a probable way to improve the SMM performance of pentacoordinated Dy-SIMs. Starting from existing systems, a rigid-scan type exploration indicates the possibility of U_{eff} higher than 1600 K.

Keywords: single-molecule magnets; ab initio calculation; crystal field analysis; axial bond angle

Academic Editor: You Song

Received: 12 December 2024
Revised: 2 January 2025
Accepted: 3 January 2025
Published: 7 January 2025

Citation: Wang, Y.-X.; Wang, Y.-F.; Yin, B. Theoretical Study of Pentacoordinated Lanthanide Single-Ion Magnets via Ab Initio Electronic Structure Calculation. *Magnetochemistry* **2025**, *11*, 3. https://doi.org/10.3390/magnetochemistry11010003

1. Introduction

Single-molecule magnets (SMMs) refer to a type of molecular systems displaying magnet behavior at the unimolecular level [1–11]. Because of their potential to retain magnetic information in one single molecule, SMMs have gained widespread attention from researchers, especially in the field of ultra-high-density storage of data [4–9]. Compared to hard-disk drives, the information storage density using SMMs can reach to 300 Tbit in^{-2}, which is up to 100 times higher [4,7]. Thus SMM could be the components in future revolutionary micro-electronic devices.

As research progresses, people have discovered the importance of lanthanide single-molecule magnets (Ln-SMMs) especially the mononuclear structures which are also called as lanthanide single-ion magnets (Ln-SIMs). Actually, many recent breakthroughs in the field of SMM are provided by Ln-SIMs [12–24]. However, a practical application of SMMs is still out of reach. As one important figure of merit of SMM, the blocking temperature (T_B) means the highest temperature to observe blocked magnetization of a sample. Until now, the record T_B values of SMMs have been within 60–80 K [10,18–21]. Although they exceed the boiling point of liquid nitrogen, these records still remain far below room temperature. Thus, enhancing the performance, e.g., increasing T_B, is one central task in the current stage of SMM.

It is well known that the coordination environment dictates the performance of SMMs, especially in the case of Ln-SIMs. Recently reducing the coordination number (CN) has been suggested to be an effective strategy for enhancing the performance of Ln-SIMs [25]. This is because a low coordination environment can lead to high magnetic axiality, which is crucial for maintaining a preferred orientation of magnetic moment to achieve a long

relaxation time. Actually, the record-holding dysprosocenium SIMs just adopt sandwiched structures presenting effective/pseudo two coordination of the central ion.

However, the SMM performances of most synthesized low CN Ln-SIMs are apparently inferior to those of dysprosocenium systems. Thus, the potential of low CN structures as high-performance SMMs has not been amply realized. The search for low CN Ln-SIMs with good SMM performance needs rational guidance, especially from theoretical studies.

Recently, the SMM performance of a group of typical low CN Ln-SIMs, i.e., tetracoordinated structures, has been well interpreted via the ab initio electronic structure calculation [26–44]. A theoretical study also indicated possible routes to improve the SMM performance and then pointed out the structures holding the possibility of T_B higher than 50 K for tetracoordinated Ln-SIMs [39].

Encouraged by its capability, ab initio electronic structure calculation is carried out here in another typical type of low CN Ln-SIMs, i.e., the pentacoordinate complexes synthesized in recent years [45–49]. Here, we selected 16 structures as the objects of this study. For the symmetry of these 16 structures, **1Dy** to **12Dy** are close to D_{4d}, and **13Dy** to **16Dy** are close to D_{3d}. In addition to interpreting the reported systems, this work also tries to give suggestions for improving the SMM performance and to predict possible improvements (Figure 1).

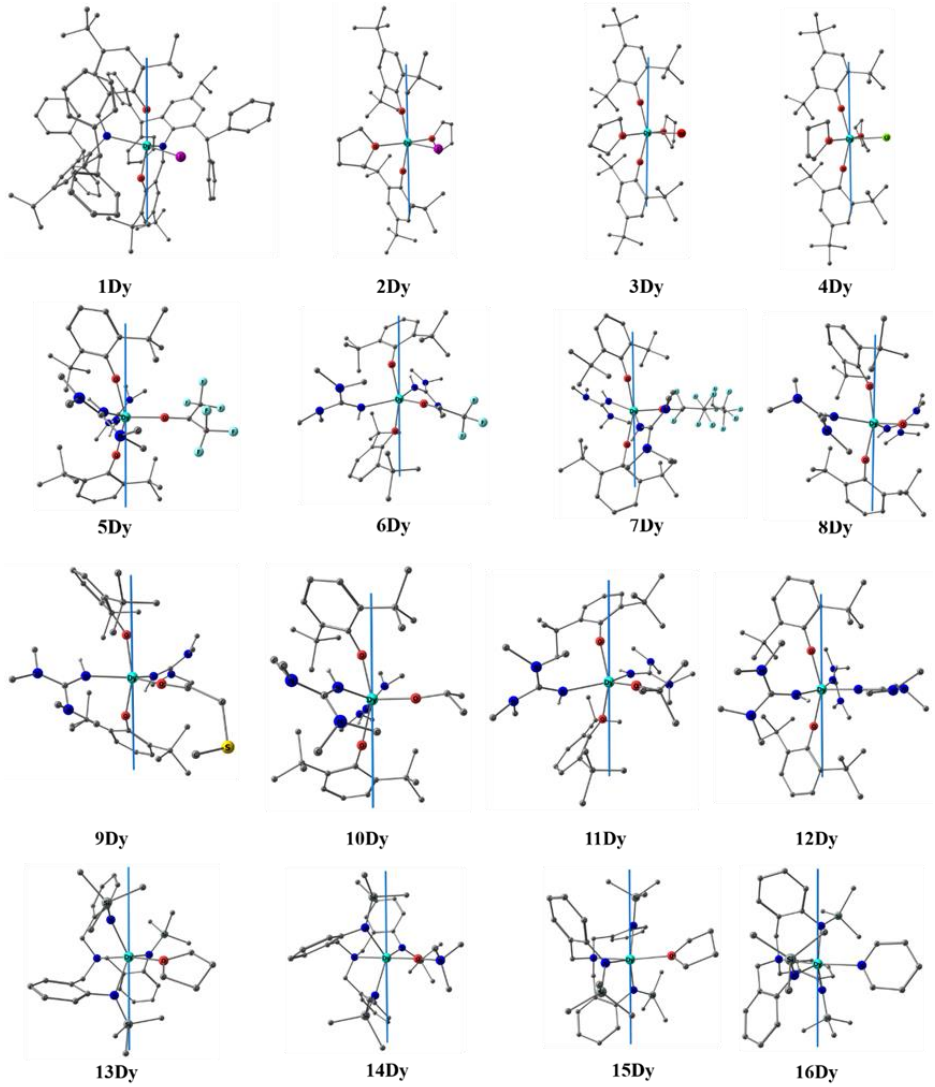

Figure 1. The structures of all SMMs involved in the study.

2. Theoretical Background and Computational Details

The microscopic mechanism underlying the SMM behavior is the magnetic relaxation at the molecular level. Due to the co-existence of several relaxation pathways, a comprehensive magnetic relaxation treatment needs to include the characteristics of the electronic and vibrational states, the coupling between them and the interaction between the system and the environment. Sophisticated methods to accomplish this task have been proposed by several groups [50–52]. However, for this type of method, huge computational cost is hardly avoidable.

Recently, a concise criterion for good SMM has been proposed to be the co-existence of long quantum tunneling of magnetization (QTM) time τ_{QTM} and a high effective barrier of magnetic reversal U_{eff} [39–43]. For Ln-SIMs, both τ_{QTM} and U_{eff} can be obtained from one single ab initio calculation for a given system. Thus, the application of this criterion is easy for a large number of Ln-SIMs due to its low computational cost [53–55]. The reliability of this criterion has been verified in structurally similar systems, e.g., tetracoordinated Ln-SIMs and square antiprism ones [39,40].

$$\tau_{QTM}^{-1} = \frac{\beta B_{ave}}{h} \cdot \frac{g_{XY}^2}{2(g_{XY}^2 + g_Z^2)^{\frac{1}{2}}},\ g_{XY} = \sqrt{g_X^2 + g_Y^2} \tag{1}$$

$$\tau_{QTM}^{-1} = \frac{\beta B_{ave}}{h} \cdot \frac{1}{2} \cdot \frac{x_{aniso}^2 g_{XY}^2}{\sqrt{x_{aniso}^2 g_{XY}^2 + (3 - 2x_{aniso}^2) g_Z^2}} \tag{2}$$

$$x_{aniso} = \frac{B_{trans}}{B_{ave}},\ B_X = B_Y = B_{trans} \tag{3}$$

The systems studied here are all Kramers SIMs of which the zero-field QTM rate τ_{QTM}^{-1}, i.e., the reciprocal of τ_{QTM}, is calculated by Equation (1). β and h in Equation (1) are the Bohr magneton and Planck constant, respectively. The principal g-factors, i.e., $g_{X\text{-}Z}$, of the ground Kramers doublet (KD) in Equation (1) are obtained from ab initio calculation. B_{ave} in Equation (1) is the averaged strength of the internal magnetic field which is empirically estimated as 20 milli Tesla (mT) here. The reliability of this selection has been proved in our previous works [39,41,42]. For field-induced systems, another parameter x_{aniso}, describing the anisotropy of the magnetic field, is needed as shown in Equations (2) and (3). Here, the applied direct current (DC) field is assumed to be added in the Z principal direction. In this case, B_X = B_Y = 20 mT and B_Z is the sum of 20 mT and the applied DC field in experiment.

$$U_{eff}(T) = \sum_i \frac{\tau_{QTM,i}^{-1,eff}(T)}{N} E_i \tag{4}$$

$$N = \sum_i \tau_{QTM,i}^{-1,eff}(T) \tag{5}$$

U_{eff} could be calculated as a weighted sum of energies of both ground and excited KDs (Equation (4)) [41,42]. The normalization factor N is the sum of the effective QTM rates of all the involved KDs (Equation (5)). The effective rate of the *i*th KD (Equation (6)) depends on its principal g-factors (Equation (7)) and the Boltzmann population (Equation (8)).

In this work, theoretical predictions of QTM time via Equations (1)–(3) and effective barrier via Equations (4)–(5) are labeled as τ_{QTM}^{Zee} and U_{eff}^{Zee} respectively. The corresponding experimental results are labeled as τ_{QTM}^{exp} and U_{eff}^{exp} respectively.

$${\tau_{QTM,i}}^{-1}(T) \propto \frac{\exp(-E_i/k_B T)}{Z} \tau_{QTM,i}^{-1,eff} \tag{6}$$

$$\tau_{\mathrm{QTM},i}^{-1,\mathrm{eff}} = \frac{g_{\mathrm{XY},i}^2}{2(g_{\mathrm{XY},i}^2 + g_{\mathrm{Z},i}^2)^{\frac{1}{2}}} \quad (7)$$

$$Z = \sum_i \exp(-E_i/k_B T) \quad (8)$$

The ab initio calculations in this work consist of two steps: first, a set of spin eigenstates are obtained via the state-averaged complete active space self-consistent field method (SA-CASSCF) [56]; then, the final states, i.e., KDs here, are obtained via state interaction which diagonalizes the spin-orbit-coupling (SOC) matrix under the basis of spin eigenstates from the first step.

A free academic version of MOLCAS 8.0 was used to perform ab initio calculation [57]. The active space consisted of 9 electrons in 7 orbitals and 21 spin sextets were included in the SA-CASSCF step [39–43]. The scalar relativistic effect was accounted via DKH2 transformation. Then, state interaction was performed via the RASSI-SO module [58], with the SOC integrals from the AMFI method [59]. We choose the ANO-RCC relativistic basis set [60,61], including VQZP for Dy, VDZP for C, VDZ for H and VTZP for the others. The SINGLE_ANISO module was used to gain the g-factors and other magnetic parameters [62,63]. The numerical results of the ab initio calculation are included in Tables S1~S16.

3. Results and Discussion

3.1. The Comparison Between Theoretical Predictions and Experimental Results

The most quoted evidence for SMM characteristics is the temperature- or frequency-dependence of the imaginary part of the alternating-current (AC) magnetic susceptibility, especially a peak. The highest temperature to observe such a peak is labeled as T_{AC} here. T_{AC} only represents the short-term magnetic memory effect and thus is less conceptually sound than a magnetic hysteresis loop or zero-field cooled susceptibility. However, T_{AC} is available for most SMMs, including all the Dy-SIMs studied here. In comparison, neither magnetic hysteresis nor zero-field cooled susceptibility holds such an availability. T_{AC} has been used to quantify T_{B} for a lot of SMMs [9]. Our recent works have also verified the capability of T_{AC} as a common measurement of SMM performance [42,64]. Thus, T_{AC} at 1000 Hz is utilized here.

As shown in Figure 2, higher T_{AC} is generally located at a position closer to the lower right corner of the plane defined by τ_{QTM} and U_{eff}. This corner just corresponds to both the longest τ_{QTM} and the highest U_{eff}. **1Dy**, which holds the highest T_{AC} here, has both the longest τ_{QTM} and the highest U_{eff} according to either theoretical prediction or experimental results (Table 1). Thus, the co-existence of longer τ_{QTM} and higher U_{eff} does correspond to better SMM performance in the pentacoordinated Ln-SIMs. The proposed criterion also works here.

Formally, this criterion only includes the QTM and thermally-activated (TA) pathways, i.e., Orbach and TA-QTM, but neglects Raman pathway. Thus, in principle, it is only necessary rather than sufficient. However, one recent in-depth statistical analysis has indicated the existence of a correlation between U_{eff} and Raman parameters, especially in high U_{eff} cases [9]. Thus, when applying the criterion, the effect of the Raman pathway might be accounted implicitly. Also, in structurally similar systems, the effect of the Raman pathway might not vary sharply [39,40].

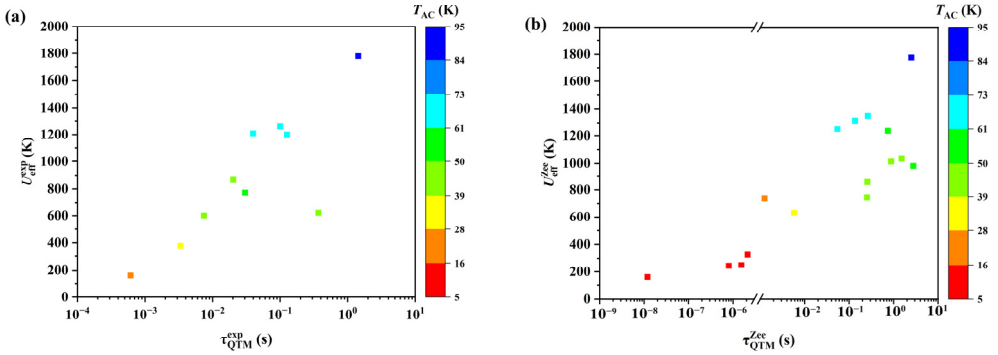

Figure 2. The relation among T_{AC}, τ_{QTM} and U_{eff}. (**a**) T_{AC} vs. experimental τ_{QTM} and U_{eff}. (**b**) T_{AC} vs. theoretical τ_{QTM} and U_{eff}.

Table 1. The experiment values and theoretical predictions of τ_{QTM} (s) and U_{eff} (K).

	Refcode	τ_{QTM}^{exp}	τ_{QTM}^{Zee}	U_{eff}^{exp}	$U_{eff}^{Zee}/U_{eff}^{KD}$	T_{AC} [a]
1Dy	LEVLEH	1.43	2.49	1780	1776/1856	95
2Dy	XUWDAX	1.26×10^{-1}	2.62×10^{-1}	1201	1350/1282	64
3Dy	XUWCUQ	3.98×10^{-2}	1.35×10^{-1}	1210	1315/1239	64
4Dy	XUWCOK	1.00×10^{-1}	5.42×10^{-2}	1262	1249/1173	64
5Dy	ENACOO	N/A [b]	7.41×10^{-1}	1176	1236/999	60
6Dy	ENACII	N/A	1.51	905	1035/964	49
7Dy	ENACUU	2.02×10^{-2}	8.77×10^{-1}	872	1014/951	41
8Dy	ENABON	3.02×10^{-2}	2.77	773	981/801	50
9Dy	ZESGAJ	3.68×10^{-1}	2.56×10^{-1}	622	859/731	45
10Dy	E.NACAA	7.45×10^{-3}	2.51×10^{-1}	601	745/684	40
11Dy	ENACEE	3.35×10^{-3}	5.75×10^{-3}	378	633/374	33
12Dy	ENABIH	6.11×10^{-4}	1.25×10^{-3}	160	738/422	22
13Dy	DEYRIO	N/A	2.12×10^{-6}	36	328/230	6
14Dy	FEYREK	N/A	1.53×10^{-6}	19	250/124	5
15Dy	DEYRIO	N/A	8.00×10^{-7}	N/A	245/0	6
16Dy	FEYRAG	4.03×10^{-4}	1.19×10^{-8}	N/A	160/0	6

[a] The highest AC frequency is usually 1000 Hz, the exception is **9Dy** (1488 Hz). [b] Data were not provided by experiments.

As shown in Figure 3, the order of either τ_{QTM}^{Zee} or U_{eff}^{Zee} is generally consistent to that of the corresponding experimental τ_{QTM}^{exp} and U_{eff}^{exp} respectively. With only one exception of **16Dy**, the deviations in τ_{QTM}^{Zee} are all less than two orders of magnitude (Figure 3a). For the SIMs holding the first four longest τ_{QTM}^{exp} here, i.e., **1Dy–4Dy**, the deviations in τ_{QTM}^{Zee} are all less than one order of magnitude. It needs to indicate that even the theoretical results from those sophisticated methods may still bear deviations of one or two orders of magnitude [53]. The large deviation in τ_{QTM}^{Zee} of field-induced **16Dy** might be attributed to the difficulty of obtaining accurate x_{aniso} [43]. As a vector field, magnetic fields have different sources, e.g., dipolar interaction with other electronic magnetic moment in the sample and hyperfine interaction due to nuclear spin [43]. Thus, the anisotropy of a magnetic field depends on both the electronic and nuclear contributions.

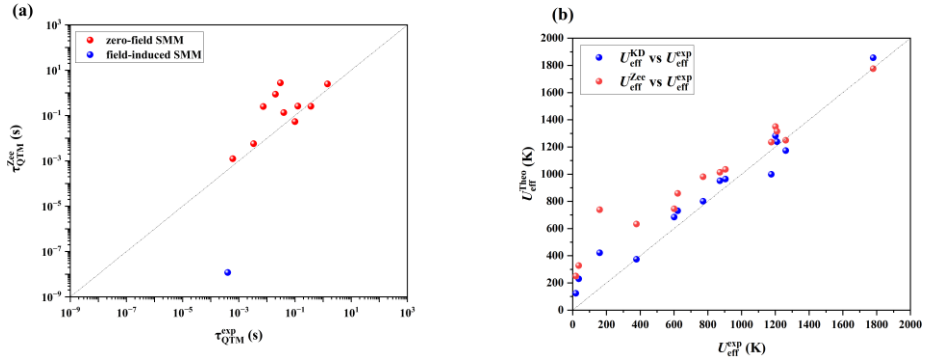

Figure 3. Comparison between theoretical prediction and experimental fitting. (**a**) τ_{QTM}^{Zee} vs. τ_{QTM}^{exp}. (**b**) U_{eff}^{Zee} vs. U_{eff}^{exp}.

In the aspect of effective barrier, we do find some large discrepancies between theoretical U_{eff}^{Zee} and experimental U_{eff}^{exp}, i.e., **11Dy–16Dy**. Their T_{AC} values are around 20 K or apparently lower (5~6 K) while other Ln-SIMs have T_{AC} values lying within the range of 40~95 K. Therefore, those large discrepancies mainly occur in systems holding inferior SMM performance as represented by low T_{AC}. In these inferior systems, pure dominance of the Orbach pathway is hardly possible and other pathways strongly drive the fitted U_{eff}^{exp} away from having a solid physical meaning [40]. Thus, in these systems, U_{eff}^{exp} becomes closer to a purely phenomenological parameter and U_{eff}^{Zee} is not obligated to be close to it [40].

Besides U_{eff}^{Zee}, we can also calculate U_{eff} as the energy of a given excited KD, identified as the most probable one wherein magnetic reversal takes place. This theoretical U_{eff} is labeled as U_{eff}^{KD} here after (Table S17 and Figure S1). As shown in Figure 4b, these two types of theoretical barrier are generally consistent with each other. They both identify that the barrier of **1Dy** is clearly higher than those of all the others.

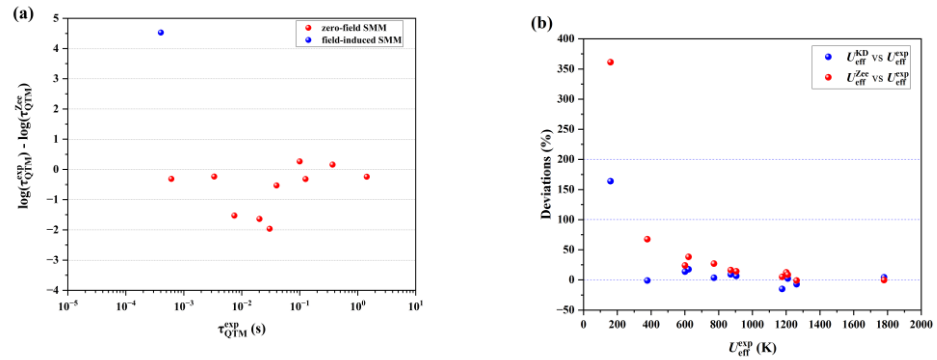

Figure 4. The deviations in τ_{QTM}^{Zee} and U_{eff}^{Zee} compared to experimental results. (**a**) Order-of-magnitude deviation in τ_{QTM}^{Zee}. (**b**) percentage deviation in U_{eff}^{Zee}.

3.2. Mechanisms of Magnetic Relaxation

According to Equation (4), U_{eff}^{Zee} can be decomposed into contributions from various KDs(Figure 5). This decomposition is capable of providing some mechanistic information about the magnetic relaxation. Since U_{eff}^{Zee} varies with the temperature value used in the calculation, two cases are analyzed for one Ln-SIM: the saturated case and the reproducing case [64]. The saturated case refers to the result when U_{eff}^{Zee} becomes a saturated value which is obtained by using 300 K in Equation (4). The reproducing case refers to the result when U_{eff}^{Zee} exactly reproduces U_{eff}^{exp} with a special temperature value T_{rep} used in Equation (4). It needs to be clarified that there is no direct relationship between T_{rep} and T_B in principle.

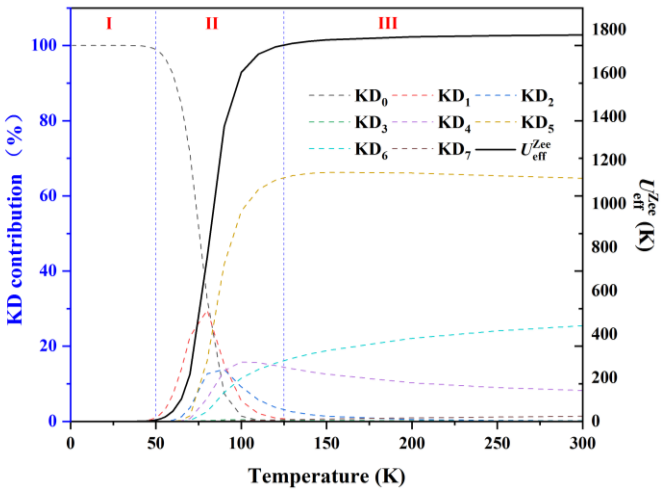

Figure 5. $U_{\mathrm{eff}}^{\mathrm{Zee}}$ and the contributions from various KDs of **1Dy**.

As shown in Table 2, the most important KDs of the saturated $U_{\mathrm{eff}}^{\mathrm{Zee}}$ of **1Dy** are KD_5 and KD_6, of which the sum contribution is 91%. These two KDs remain to be the most important ones (68%) in the reproducing case while KD_4 (16%) also plays a role. Thus, the most important KDs of U_{eff} of **1Dy** are some highly excited ones which do not change heavily between the saturated case and the reproducing case. The contributions from the ground and other lower excited KDs are negligible. These results suggest that, in **1Dy**, the slow thermally-activated relaxation, proceeding mainly via KD_5 and KD_6, is important while the ground KD QTM is not efficient. This is consistent to the long τ_{QTM} and high U_{eff} and T_{AC} of **1Dy**. Similar results occur in **2Dy**–**5Dy**.

Table 2. The contributions of various KDs to U_{eff} in the saturated and reproducing cases.

	Saturated Case	Reproducing Case	T_{rep}
1Dy	KD5 + KD6 (91%)	KD5 + KD6 (68%), KD4 (16%)	100 [a]
2Dy	KD3 + KD4 (97%)	KD4 + KD3 (82%)	79
3Dy	KD3 + KD4 (95%)	KD3 + KD4 (77%), KD2 (21%)	86
4Dy	KD3 + KD4 (96%)	KD3 + KD4 (86%)	90 [a]
5Dy	KD4 + KD5 + KD6 (79%)	KD4 + KD5 + KD6 (75%), KD3 (15%)	160
6Dy	KD3 (38%) + KD5 (36%) + KD4 (18%)	KD3 (47%) + KD0 (28%) + KD2 (11%)	49
7Dy	KD4 (53%) + KD5 (28%) + KD6 (16%)	KD4 (62%) + KD1 (9%) + KD5 (8%)	56
8Dy	KD3 (42%) + KD5 (38%) + KD4 (12%)	KD3 (52%) + KD2 (19%) + KD0 (13%)	48
9Dy	KD5 (40%) + KD3 (38%) + KD2 (15%)	KD2 (48%) + KD3 (25%) + KD0 (18%)	44
10Dy	KD2 (46%) + KD3 (35%) + KD4 (18%)	KD2 (71%) + KD0 (15%) + KD3 (12%)	38
11Dy	KD3 (53%) + KD2 (43%)	KD2 (54%) + KD0 (25%) + KD3 (12%)	40
12Dy	KD3 (52%) + KD2 (16%) + KD7 (12%)	KD0 (74%) + KD3 (13%)	42
13Dy	KD2 (48%) + KD1 (39%) + KD3 (10%)	KD0 (83%) + KD1 (16%)	31
14Dy	KD3 (66%) + KD4 (14%)	KD0 (86%) + KD1 (13%)	23
15Dy	KD1 (70%) + KD2 (21%)	N/A [b]	N/A
16Dy	KD1 (44%) + KD2 (30%) + KD0 (16%)	N/A	N/A

[a] In these cases, the saturated theoretical barrier is still a little bit lower than the experimentally fitted one. Thus, T_{rep} in these cases is taken as the temperature at 2/3 position of region II. [b] $U_{\mathrm{eff}}^{\mathrm{exp}}$ were not provided by experiments.

For other Ln-SIMs' U_{eff}, the contributions from the lower excited KDs and even the ground KD_0 are more important. In some reproducing cases, i.e., **12Dy–14Dy**, KD_0 even becomes the most important one. These results support a smaller contribution from slow thermally activated relaxation and a larger contribution from fast ground KD QTM. This is consistent with their inferior SMM performance as represented by lower T_{AC} when compared to **1Dy–5Dy**.

3.3. Crystal-Field Analysis and Theoretical Magneto-Structural Correlation

Since 20 mT B_{ave} is used for most Ln-SIMs here, their SMM performance ought to be mainly dictated by the principal g-factors and energies of the KDs. These are all determined by the electronic structure. The crystal field (CF) Hamiltonian (Equation (9)) is a suitable theoretical tool for interpreting the electronic structure of Ln-SIMs. Since O_k^q are common operators, the electronic structure characteristics arise solely from the CF parameter (CFP) B_k^q [11,30,41,65].

Accurate CFPs could be extracted from ab initio results via irreducible tensor operator (ITO). The point charge electrostatic model (PCEM) can also help to give a rough estimate of CFPs as a sum of contributions from the coordinating atoms (Equation (10)) [65]. Z_{eff} and R_j in Equation (10) are the effective charge and distance to the central ion of a given coordinating atom j respectively. Y_k^q is the spherical harmonic function of which the variables are azimuthal coordinates θ_j and ϕ_j of the coordinating atoms.

$$\hat{H}_{CF} = \sum_{k=2,4,6} \sum_{q=-k}^{k} B_k^q \hat{O}_k^q(\hat{\vec{J}}) \tag{9}$$

$$\left|B_k^q\right| \sim \sum_{j}^{\text{ligand}} \left\{ \frac{Z_{\text{eff},j}}{R_j^{k+1}} Y_k^q(\theta_j, \phi_j) \right\} \tag{10}$$

It must be clarified that Equation (10) only provides a rough estimate of the relative magnitude of CFPs rather than the actual value. The PCEM estimate does not even have the unit of energy. It also neglects the covalent contribution which has been shown to be capable of playing an important role recently [66,67]. However, there are some advantages of the PCEM estimate. First, as it is related to the position and charge of the coordinating atoms, it is chemically intuitive [39–41]. Second, it can help measuring the importance of different coordinating atoms since it is a sum of atomic contributions.

In principle, CFPs up to at least $k = 6$ need to be included. However, recent works have indicated that 2nd-rank CFPs, especially the diagonal term B_2^0, can be the leading ones to give a reasonable explanation by themselves [64]. All the ITO B_2^0 are negative and hence we only need to discuss their magnitude, as indicated by their absolute values $|B_2^0|$.

As shown in Figure 6, a larger $|B_2^0|$ usually corresponds to higher T_{AC} or U_{eff}. The best SMM here, **1Dy** (T_{AC} = 95 K), holds the largest $|B_2^0|$ (Table S18). **2Dy–4Dy** also have a high T_{AC} (86 K) and their $|B_2^0|$ values, are slightly smaller than that of **1Dy** but clearly larger than all the others. Although being less accurate, the PCEM estimate also captures the general trend (Figure 6 and Table S18) and thus subsequent PCEM analysis should be reliable.

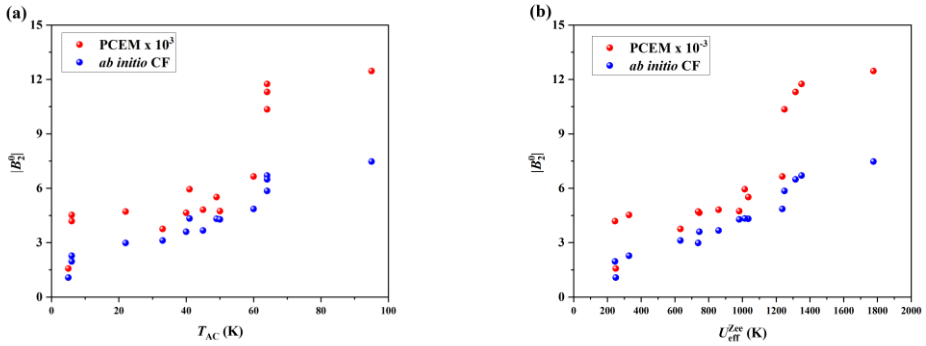

Figure 6. Crystal field analysis based on both ab initio ITO and PCEM. (**a**) T_{AC} vs. $|B_2^0|$ in the studied systems. (**b**) U_{eff}^{Zee} vs. $|B_2^0|$ in the studied systems.

Based on their positions with respect to the magnetic easy axis, the coordinating atoms could be divided into two types: the axial ones lying close to the easy axis and the equatorial ones perpendicular to the easy axis (Table S20) [65]. PCEM suggests that the contribution from axial atoms tends to increase $|B_2^0|$ while that from equatorial atoms is destructive.

1Dy holds the largest PCEM estimate of $|B_2^0|$ but its contribution from the two axial atoms is even smaller than that of **2Dy** (Table S20). Interestingly the amount of destructive contribution from the equatorial atoms of **1Dy** (-4.45×10^{-3}) is clearly smaller than that of **2Dy** (-5.39×10^{-3}). This smaller destructive contribution is one important reason for the largest PCEM estimate of $|B_2^0|$ of **1Dy**. Although **3Dy** has the largest constructive contribution to $|B_2^0|$ from the axial coordinating atoms (Table S20), its destructive contribution from equatorial atoms is also larger than that of **1Dy**. Thus, the eventual $|B_2^0|$ of 3Dy is smaller than that of **1Dy**.

For the Dy-SIMs studied here, the bond angle between the central Ln ion and two axial atoms is around 150°. A previous study of tetracoordinated Ln-SIMs has indicated that widening this angle can improve the SMM performance significantly [39]. Linear or quasi-linear O–Dy–O arrangement will facilitate the generation of high magnetic axiality due to the oblate shape of the electron density of the ground state of the central Dy^{III} ion. This widening might be made possible by applying pressure [68]. The two axial O atoms of **1Dy** come from the same bidentate ligand HL (2-((2,6-dibenzhydryl-4-isopropylphenylimino)methyl)-4,6-di-*tret*-butylphenol) and thus widening of the axial bond angle is probably restricted there. Consequently, we chose to explore **2Dy** and **5Dy** wherein only monodentate ligands were involved. This exploration was performed in a rigid-scan way wherein only the axial bond angle is varied. Clearly this rigid-scan exploration has limited precision, and the results only provide some possibility. However, the capability of rigid-scan has already been verified in our recent work on Ln-SIMs [39].

As show in Figure 7, widening ∠O–Dy–O up to 180° can lead to an increase in τ_{QTM} by one order of magnitude, i.e., from around 0.25 s to around 2.75 s. Meanwhile, U_{eff} also experiences a sharp increase by about 600 K, from ~1300 K (150°) to ~1900 K (180°). For **5Dy**, there is no significant change in τ_{QTM} with widening ∠O–Dy–O. Meanwhile, U_{eff} increases by about 400 K from around 1200 K (150°) to around 1600 K (180°). Thus, starting from the reported pentacoordiated Ln-SIMs, widening the axial bond angle might be a probable way to improve the SMM performance.

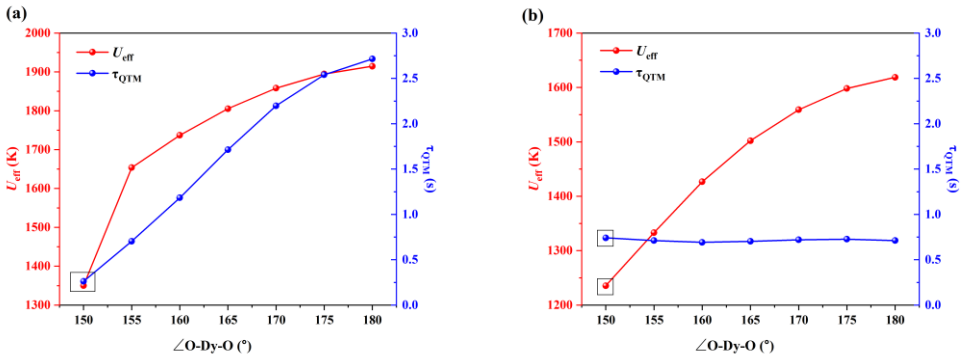

Figure 7. Theoretical prediction of two structures in a rigid-scan way. (**a**) τ_{QTM} and U_{eff} along ∠O–Dy–O of **2Dy**. (**b**) τ_{QTM} and U_{eff} along ∠O–Dy–O of **5Dy**.

4. Conclusions

A theoretical study, based on ab initio electronic structure calculation, was carried out in a group of 16 pentacoordinate Dy-SIMs. The experimentally observed SMM performance is well explained by a concise criterion, i.e., the co-existence of τ_{QTM} and U_{eff}.

Crystal field analysis indicated that 2nd-rank CFPs, especially the diagonal term B_2^0, are the leading ones to generate the desired electronic structure favoring good SMM performance. To have the needed CFPs, the contribution from the equatorial coordinating atoms might be even more important than that from the axial coordinating atoms.

Widening the axial bond angle between the central Ln ion and two axial atoms might be a probable way to improve the SMM performance of pentacoordinated Ln-SIMs. Starting from existing systems, a rigid-scan type exploration indicates the possibility of U_{eff} higher than 1600 K.

Supplementary Materials: The following supporting information can be downloaded at: https://www.mdpi.com/article/10.3390/magnetochemistry11010003/s1, Table S1. ab initio results of 1Dy (LEVLEH); Table S2. ab initio results of 2Dy (XUWDAX); Table S3. ab initio results of **3Dy** (XUWCUQ); Table S4. ab initio results of **4Dy** (XUWCOK); Table S5. ab initio results of **5Dy** (ENACII); Table S6. ab initio results of **6Dy** (ENACII); Table S7. ab initio results of **7Dy** (ENACUU); Table S8. ab initio results of **8Dy** (ENABON); Table S9. ab initio results of **9Dy** (ZESGAJ); Table S10. ab initio results of **10Dy** (ENACAA); Table S11. ab initio results of **11Dy** (ENACEE); Table S12. ab initio results of **12Dy** (ENABIH); Table S13. ab initio results of **13Dy** (DEYRIO); Table S14. ab initio results of **14Dy** (FEYREK); Table S15. ab initio results of **15Dy** (DEYRIO); Table S16. ab initio results of **16Dy** (FEYRAG); Table S17. Various U_{eff}^{KD} values according to transition magnetic moment |μ|, angle of easy axis of excited KD with respect to that of ground KD (θ) and crystal field wave function composition; Table S18. ab initio and PCEM crystal field parameters (in cm^{-1} and a.u. respectively) of Dy-SIMs [a]; Table S19. The distance R to Dy^{3+} (in Å), atomic charge Z_{eff} (in |*e*|) and angle θ, ϕ with respect to the ab initio magnetic easy axis (in °) of atoms in the first sphere; Table S20. The average distance R to Dy^{3+} (in Å), average atomic charge Z_{eff} (in |*e*|), average angle θ with respect to the ab initio magnetic easy axis (in °) and contribution to $|B_2^0|$ from the atoms in the first sphere; Table S21. Theoretical prediction of 2Dy τ_{QTM} and U_{eff} with different ∠O–Dy–O; Table S22. Theoretical prediction of **5Dy** τ_{QTM} and U_{eff} with different ∠O–Dy–O; Table S23. Cartesian coordinates of complexes; Figure S1. Possible relaxation mechanism based on transition magnetic moment for the Ln-SIMs studied here; Figure S2. U_{eff}^{Zee} and the contributions from various KDs of other SIMs.

Author Contributions: Conceptualization, B.Y.; Formal analysis, Y.-X.W. and B.Y.; Investigation, Y.-X.W. and Y.-F.W.; Resources, B.Y.; Writing—original draft, Y.-X.W.; Writing—review & editing, B.Y.; Supervision, B.Y.; Project administration, B.Y. All authors have read and agreed to the published version of the manuscript.

Funding: This work is supported by the National Natural Science Foundation of China (No. 22373076).

Data Availability Statement: The original contributions presented in this study are included in the article/Supplementary Material. Further inquiries can be directed to the corresponding author.

Acknowledgments: We thank Yuanhe Huang and De-Cai Fang (Beijing Normal University) for their long-term support and encouragement.

Conflicts of Interest: The authors declare no conflicts of interest.

References

1. Sessoli, R.; Gatteschi, D.; Caneschi, A.; Novak, M.A. Magnetic bistability in a metal-ion cluster. *Nature* **1993**, *365*, 141–143. [CrossRef]
2. Sessoli, R.; Tsai, H.L.; Schake, A.R.; Wang, S.; Vincent, J.B.; Folting, K.; Gatteschi, D.; Christou, G.; Hendrickson, D.N. High-spin molecules: $[Mn_{12}O_{12}(O_2CR)_{16}(H_2O)_4]$. *J. Am. Chem. Soc.* **1993**, *115*, 1804–1816. [CrossRef]
3. Gatteschi, D.; Sessoli, R.; Villain, J. *Molecular Nanomagnets*; Oxford University Press: New York, NY, USA, 2006. [CrossRef]
4. Liddle, S.T.; van Slageren, J. Improving f-element single molecule magnets. *Chem. Soc. Rev.* **2015**, *44*, 6655–6669. [CrossRef] [PubMed]
5. Liu, J.-L.; Chen, Y.-C.; Tong, M.-L. Symmetry strategies for high performance lanthanide-based single-molecule magnets. *Chem. Soc. Rev.* **2018**, *47*, 2431–2453. [CrossRef]
6. Parmar, V.S.; Mills, D.P.; Winpenny, R.E.P. Mononuclear Dysprosium Alkoxide and Aryloxide Single-Molecule Magnets. *Chem. Eur. J.* **2021**, *27*, 7625–7645. [CrossRef] [PubMed]
7. Zabala-Lekuona, A.; Seco, J.M.; Colacio, E. Single-Molecule Magnets: From Mn12-ac to dysprosium metallocenes, a travel in time. *Coord. Chem. Rev.* **2021**, *441*, 213984. [CrossRef]
8. Chilton, N.F. Molecular Magnetism. *Annu. Rev. Mater. Res.* **2022**, *52*, 79–101. [CrossRef]
9. Duan, Y.; Rosaleny, L.E.; Coutinho, J.T.; Giménez-Santamarina, S.; Scheie, A.; Baldoví, J.J.; Cardona-Serra, S.; Gaita-Ariño, A. Data-driven design of molecular nanomagnets. *Nat. Commun.* **2022**, *13*, 7626. [CrossRef] [PubMed]
10. Gould, C.A.; McClain, K.R.; Reta, D.; Kragskow, J.G.C.; Marchiori, D.A.; Lachman, E.; Choi, E.-S.; Analytis, J.G.; Britt, R.D.; Chilton, N.F.; et al. Ultrahard magnetism from mixed-valence dilanthanide complexes with metal-metal bonding. *Science* **2022**, *375*, 198–202. [CrossRef] [PubMed]
11. Ungur, L.; Chibotaru, L.F. Strategies toward High-Temperature Lanthanide-Based Single-Molecule Magnets. *Inorg. Chem.* **2016**, *55*, 10043–10056. [CrossRef]
12. Jiang, S.-D.; Wang, B.-W.; Su, G.; Wang, Z.-M.; Gao, S. A Mononuclear Dysprosium Complex Featuring Single-Molecule-Magnet Behavior. *Angew. Chem. Int. Ed.* **2010**, *49*, 7448–7451. [CrossRef]
13. Ungur, L.; Le Roy, J.J.; Korobkov, I.; Murugesu, M.; Chibotaru, L.F. Fine-tuning the Local Symmetry to Attain Record Blocking Temperature and Magnetic Remanence in a Single-Ion Magnet. *Angew. Chem. Int. Ed.* **2014**, *53*, 4413–4417. [CrossRef]
14. Gupta, S.K.; Rajeshkumar, T.; Rajaraman, G.; Murugavel, R. An air-stable Dy(III) single-ion magnet with high anisotropy barrier and blocking temperature. *Chem. Sci.* **2016**, *7*, 5181–5191. [CrossRef]
15. Liu, J.; Chen, Y.-C.; Liu, J.-L.; Vieru, V.; Ungur, L.; Jia, J.-H.; Chibotaru, L.F.; Lan, Y.; Wernsdorfer, W.; Gao, S.; et al. A Stable Pentagonal Bipyramidal Dy(III) Single-Ion Magnet with a Record Magnetization Reversal Barrier over 1000 K. *J. Am. Chem. Soc.* **2016**, *138*, 5441–5450. [CrossRef] [PubMed]
16. Chen, Y.-C.; Liu, J.-L.; Ungur, L.; Liu, J.; Li, Q.-W.; Wang, L.-F.; Ni, Z.-P.; Chibotaru, L.F.; Chen, X.-M.; Tong, M.-L. Symmetry-Supported Magnetic Blocking at 20 K in Pentagonal Bipyramidal Dy(III) Single-Ion Magnets. *J. Am. Chem. Soc.* **2016**, *138*, 2829–2837. [CrossRef] [PubMed]
17. Feng, M.; Tong, M.-L. Single Ion Magnets from 3d to 5f: Developments and Strategies. *Chem. Eur. J.* **2018**, *24*, 7574–7594. [CrossRef]
18. Goodwin, C.A.P.; Ortu, F.; Reta, D.; Chilton, N.F.; Mills, D.P. Molecular magnetic hysteresis at 60 kelvin in dysprosocenium. *Nature* **2017**, *548*, 439–442. [CrossRef] [PubMed]
19. Guo, F.-S.; Day, B.M.; Chen, Y.-C.; Tong, M.-L.; Mansikkamäki, A.; Layfield, R.A. Magnetic hysteresis up to 80 kelvin in a dysprosium metallocene single-molecule magnet. *Science* **2018**, *362*, 1400–1403. [CrossRef]
20. Vanjak, J.C.; Wilkins, B.O.; Vieru, V.; Bhuvanesh, N.S.; Reibenspies, J.H.; Martin, C.D.; Chibotaru, L.F.; Nippe, M. A High-Performance Single-Molecule Magnet Utilizing Dianionic Aminoborolide Ligands. *J. Am. Chem. Soc.* **2022**, *144*, 17743–17747. [CrossRef] [PubMed]
21. Vincent, A.H.; Whyatt, Y.L.; Chilton, N.F.; Long, J.R. Strong Axiality in a Dysprosium(III) Bis(borolide) Complex Leads to Magnetic Blocking at 65 K. *J. Am. Chem. Soc.* **2023**, *145*, 1572–1579. [CrossRef]
22. Zhu, Z.; Zhao, C.; Feng, T.; Liu, X.; Ying, X.; Li, X.-L.; Zhang, Y.-Q.; Tang, J. Air-Stable Chiral Single-Molecule Magnets with Record Anisotropy Barrier Exceeding 1800 K. *J. Am. Chem. Soc.* **2021**, *143*, 10077–10082. [CrossRef] [PubMed]

23. Wang, H.-S.; Zhang, K.; Wang, J.; Hu, Z.; Song, Y.; Zhang, Z.; Pan, Z.-Q. Regulating the distortion degree of the square antiprism coordination geometry in Dy–Na single ion magnets. *CrystEngComm* **2021**, *23*, 3175–3184. [CrossRef]
24. Wang, H.-S.; Zhang, K.; Wang, J.; Hu, Z.-B.; Zhang, Z.; Song, Y.; Zhang, Y.-Q. Influence of the Different Types of Auxiliary Noncarboxylate Organic Ligands on the Topologies and Magnetic Relaxation Behavior of Zn–Dy Heterometallic Single Molecule Magnets. *Inorg. Chem.* **2021**, *60*, 9941–9955. [CrossRef] [PubMed]
25. Ungur, L.; Chibotaru, L.F. Magnetic anisotropy in the excited states of low symmetry lanthanide complexes. *Phys. Chem. Chem. Phys.* **2011**, *13*, 20086–20090. [CrossRef] [PubMed]
26. Chilton, N.F.; Goodwin, C.A.P.; Mills, D.P.; Winpenny, R.E.P. The first near-linear bis(amide) f-block complex: A blueprint for a high temperature single molecule magnet. *Chem. Commun.* **2015**, *51*, 101–103. [CrossRef] [PubMed]
27. Chilton, N.F. Design Criteria for High-Temperature Single-Molecule Magnets. *Inorg. Chem.* **2015**, *54*, 2097–2099. [CrossRef]
28. Luzon, J.; Sessoli, R. Lanthanides in molecular magnetism: So fascinating, so challenging. *Dalton Trans.* **2012**, *41*, 13556–13567. [CrossRef] [PubMed]
29. Ungur, L.; Thewissen, M.; Costes, J.-P.; Wernsdorfer, W.; Chibotaru, L.F. Interplay of Strongly Anisotropic Metal Ions in Magnetic Blocking of Complexes. *Inorg. Chem.* **2013**, *52*, 6328–6337. [CrossRef] [PubMed]
30. Chibotaru, L.F. Theoretical Understanding of Anisotropy in Molecular Nanomagnets. In *Molecular Nanomagnets and Related Phenomena*; Gao, S., Ed.; Springer: Berlin/Heidelberg, Germany, 2015; pp. 185–229.
31. Ungur, L.; Chibotaru, L.F. Computational Modelling of the Magnetic Properties of Lanthanide Compounds. In *Lanthanides and Actinides in Molecular Magnetism*; Wiley: Hoboken, New Jersey, USA, 2015. [CrossRef]
32. Gómez-Coca, S.; Aravena, D.; Morales, R.; Ruiz, E. Large magnetic anisotropy in mononuclear metal complexes. *Coord. Chem. Rev.* **2015**, *289–290*, 379–392. [CrossRef]
33. Baldoví, J.J.; Duan, Y.; Morales, R.; Gaita-Ariño, A.; Ruiz, E.; Coronado, E. Rational Design of Lanthanoid Single-Ion Magnets: Predictive Power of the Theoretical Models. *Chem. Eur. J.* **2016**, *22*, 13532–13539. [CrossRef]
34. Gupta, T.; Rajaraman, G. Modelling spin Hamiltonian parameters of molecular nanomagnets. *Chem. Commun.* **2016**, *52*, 8972–9008. [CrossRef] [PubMed]
35. Ungur, L. 1—Introduction to the electronic structure, luminescence, and magnetism of lanthanides. In *Lanthanide-Based Multifunctional Materials*; Martín-Ramos, P., Ramos Silva, M., Eds.; Elsevier: Amsterdam, The Netherlands, 2018; pp. 1–58.
36. Kotrle, K.; Herchel, R. Are Inorganic Single-Molecule Magnets a Possibility? A Theoretical Insight into Dysprosium Double-Deckers with Inorganic Ring Systems. *Inorg. Chem.* **2019**, *58*, 14046–14057. [CrossRef]
37. Castro-Alvarez, A.; Gil, Y.; Llanos, L.; Aravena, D. High performance single-molecule magnets, Orbach or Raman relaxation suppression? *Inorg. Chem. Front.* **2020**, *7*, 2478–2486. [CrossRef]
38. Aravena, D.; Ruiz, E. Spin dynamics in single-molecule magnets and molecular qubits. *Dalton Trans.* **2020**, *49*, 9916–9928. [CrossRef]
39. Yang, Q.-Q.; Wang, Y.-F.; Wang, Y.-X.; Tang, M.-J.; Yin, B. Ab initio prediction of key parameters and magneto-structural correlation of tetracoordinated lanthanide single-ion magnets. *Phys. Chem. Chem. Phys.* **2023**, *25*, 18387–18399. [CrossRef] [PubMed]
40. Liu, H.; Li, J.-F.; Yin, B. The coexistence of long τ_{QTM} and high U_{eff} as a concise criterion for a good single-molecule magnet: A theoretical case study of square antiprism dysprosium single-ion magnets. *Phys. Chem. Chem. Phys.* **2022**, *24*, 11729–11742. [CrossRef] [PubMed]
41. Wu, X.; Li, J.-F.; Yin, B. The interpretation and prediction of lanthanide single-ion magnets from ab initio electronic structure calculation: The capability and limit. *Dalton Trans.* **2022**, *51*, 14793–14816. [CrossRef] [PubMed]
42. Yin, B.; Li, C.-C. A method to predict both the relaxation time of quantum tunneling of magnetization and the effective barrier of magnetic reversal for a Kramers single-ion magnet. *Phys. Chem. Chem. Phys.* **2020**, *22*, 9923–9933. [CrossRef] [PubMed]
43. Yin, B.; Luo, L. The anisotropy of the internal magnetic field on the central ion is capable of imposing great impact on the quantum tunneling of magnetization of Kramers single-ion magnets. *Phys. Chem. Chem. Phys.* **2021**, *23*, 3093–3105. [CrossRef] [PubMed]
44. Dergachev, V.D.; Nakritskaia, D.D.; Varganov, S.A. Strong Relativistic Effects in Lanthanide-Based Single-Molecule Magnets. *J. Phys. Chem. Lett.* **2022**, *13*, 6749–6754. [CrossRef] [PubMed]
45. Zhu, Z.; Zhang, Y.-Q.; Li, X.-L.; Guo, M.; Lu, J.; Liu, S.; Layfield Richard, A.; Tang, J. Tuning Magnetic Relaxation in Square-Pyramidal Dysprosium Single-Molecule Magnets Using Apical Alkoxide Ligands. *CCS Chem.* **2021**, *3*, 388–398. [CrossRef]
46. Guo, Y.; Liu, K.; Qin, Y.; Wu, Q.; Hu, K.; Mei, L.; Chai, Z.; Liu, X.; Yu, J.; Shi, W. Role of molecular symmetry in the magnetic relaxation dynamics of five-coordinate Dy(iii) complexes. *Dalton Trans.* **2023**, *52*, 2703–2711. [CrossRef]
47. Zhu, Z.; Ying, X.; Zhao, C.; Zhang, Y.-Q.; Tang, J. A new breakthrough in low-coordinate Dy(iii) single-molecule magnets. *Inorg. Chem. Front.* **2022**, *9*, 6061–6066. [CrossRef]
48. Parmar, V.S.; Ortu, F.; Ma, X.; Chilton, N.F.; Clérac, R.; Mills, D.P.; Winpenny, R.E.P. Probing Relaxation Dynamics in Five-Coordinate Dysprosium Single-Molecule Magnets. *Chem. Eur. J.* **2020**, *26*, 7774–7778. [CrossRef]
49. Ying, X.; Zhu, Z.; Zhao, C.; Zhang, Y.-Q.; Tang, J. Five-Coordinated Dysprosium Single-Molecule Magnet Functionalized by the SMe Group. *Inorg. Chem.* **2022**, *61*, 20547–20551. [CrossRef] [PubMed]

50. Bartolomé, E.; Arauzo, A.; Luzón, J.; Bartolomé, J.; Bartolomé, F. Chapter 1—Magnetic Relaxation of Lanthanide-Based Molecular Magnets. In *Handbook of Magnetic Materials*; Brück, E., Ed.; Elsevier: Amsterdam, The Netherlands, 2017; Volume 26, pp. 1–289.
51. Gatteschi, D.; Sessoli, R. Quantum Tunneling of Magnetization and Related Phenomena in Molecular Materials. *Angew. Chem. Int. Ed.* **2003**, *42*, 268–297. [CrossRef] [PubMed]
52. Garanin, D.A.; Chudnovsky, E.M. Thermally activated resonant magnetization tunneling in molecular magnets: $Mn_{12}Ac$ and others. *Physical Review B* **1997**, *56*, 11102–11118. [CrossRef]
53. Lunghi, A.; Sanvito, S. Computational design of magnetic molecules and their environment using quantum chemistry, machine learning and multiscale simulations. *Nat. Rev. Chem.* **2022**, *6*, 761–781. [CrossRef] [PubMed]
54. Reta, D.; Kragskow, J.G.C.; Chilton, N.F. Ab Initio Prediction of High-Temperature Magnetic Relaxation Rates in Single-Molecule Magnets. *J. Am. Chem. Soc.* **2021**, *143*, 5943–5950. [CrossRef] [PubMed]
55. Briganti, M.; Santanni, F.; Tesi, L.; Totti, F.; Sessoli, R.; Lunghi, A. A Complete Ab Initio View of Orbach and Raman Spin–Lattice Relaxation in a Dysprosium Coordination Compound. *J. Am. Chem. Soc.* **2021**, *143*, 13633–13645. [CrossRef] [PubMed]
56. Roos, B.O.; Taylor, P.R.; Sigbahn, P.E.M. A complete active space SCF method (CASSCF) using a density matrix formulated super-CI approach. *Chem. Phys.* **1980**, *48*, 157–173. [CrossRef]
57. Aquilante, F.; Autschbach, J.; Carlson, R.K.; Chibotaru, L.F.; Delcey, M.G.; De Vico, L.; Fdez Galván, I.; Ferré, N.; Frutos, L.M.; Gagliardi, L.; et al. Molcas 8: New capabilities for multiconfigurational quantum chemical calculations across the periodic table. *J. Comput. Chem.* **2016**, *37*, 506–541. [CrossRef]
58. Malmqvist, P.Å.; Roos, B.O.; Schimmelpfennig, B. The restricted active space (RAS) state interaction approach with spin–orbit coupling. *Chem. Phys. Lett.* **2002**, *357*, 230–240. [CrossRef]
59. Heß, B.A.; Marian, C.M.; Wahlgren, U.; Gropen, O. A mean-field spin-orbit method applicable to correlated wavefunctions. *Chem. Phys. Lett.* **1996**, *251*, 365–371. [CrossRef]
60. Roos, B.O.; Lindh, R.; Malmqvist, P.-Å.; Veryazov, V.; Widmark, P.-O. Main Group Atoms and Dimers Studied with a New Relativistic ANO Basis Set. *J. Phys. Chem. A* **2004**, *108*, 2851–2858. [CrossRef]
61. Roos, B.O.; Lindh, R.; Malmqvist, P.-Å.; Veryazov, V.; Widmark, P.-O.; Borin, A.C. New Relativistic Atomic Natural Orbital Basis Sets for Lanthanide Atoms with Applications to the Ce Diatom and LuF_3. *J. Phys. Chem. A* **2008**, *112*, 11431–11435. [CrossRef]
62. Chibotaru, L.F.; Ungur, L. Ab initio calculation of anisotropic magnetic properties of complexes. I. Unique definition of pseudospin Hamiltonians and their derivation. *J. Chem. Phys.* **2012**, *137*, 064112. [CrossRef]
63. Chibotaru, L.F. Ab Initio Methodology for Pseudospin Hamiltonians of Anisotropic Magnetic Complexes. *Adv. Chem. Phys.* **2013**, *153*, 397–519.
64. Wang, Y.-F.; Wang, Y.-X.; Yang, Q.-Q.; Yin, B. Auxiliary Rather Than Dominant. The Role of Direct Dy–S Coordination in Single-Molecule Magnet Unveiled via ab initio Study. *J. Phys. Chem. A* **2024**, *128*, 5285–5297. [CrossRef] [PubMed]
65. Ungur, L.; Chibotaru, L.F. Ab Initio Crystal Field for Lanthanides. *Chem. Eur. J.* **2017**, *23*, 3708–3718. [CrossRef] [PubMed]
66. Briganti, M.; Garcia, G.F.; Jung, J.; Sessoli, R.; Le Guennic, B.; Totti, F. Covalency and magnetic anisotropy in lanthanide single molecule magnets: The DyDOTA archetype. *Chem. Sci.* **2019**, *10*, 7233–7245. [CrossRef] [PubMed]
67. Manvell, A.S.; Pfleger, R.; Bonde, N.A.; Briganti, M.; Mattei, C.A.; Nannestad, T.B.; Weihe, H.; Powell, A.K.; Ollivier, J.; Bendix, J.; et al. LnDOTA puppeteering: Removing the water molecule and imposing tetragonal symmetry. *Chem. Sci.* **2024**, *15*, 113–123. [CrossRef] [PubMed]
68. Pointillart, F.; Le Guennic, B.; Cador, O. Pressure-Induced Structural, Optical and Magnetic Modifications in Lanthanide Single-Molecule Magnets. *Chem. Eur. J.* **2024**, *30*, e202400610. [CrossRef] [PubMed]